Independent University **Bangladesh (IUB)**

IUB Academic Repository

Electrical and Electronics Engineering Article

2014-04-15

Artifact Characterization and Removal for In-Vivo Neural Recording

Islam, Md Kafiul

Elsevier

http://dir.iub.edu.bd:8180/handle/123456789/262

Downloaded from IUB Academic Repository

Journal of Neuroscience Methods 226 (2014) 110–123

Contents lists available at ScienceDirect

Journal of Neuroscience Methods

journal homepage: www.elsevier.com/locate/jneumeth

Computational Neuroscience

Artifact characterization and removal for *in vivo* neural recording

Md Kafiul Islam[a,*], Amir Rastegarnia[a,b], Anh Tuan Nguyen[a], Zhi Yang[a]

[a] Department of Electrical and Computer Engineering, National University of Singapore, Singapore 117583, Singapore
[b] Department of Electrical Engineering, Malayer University, Malayer 95863-65719, Iran

HIGHLIGHTS

- We characterize labeled artifacts in neural recording experiments.
- An algorithm for automatic artifact detection and removal is proposed.
- A modified universal-threshold value is proposed to make the algorithm robust under different recording conditions.
- Both real and synthesized data have been used for testing the proposed algorithm in comparison with other available algorithms.
- Quantitative results show that the proposed algorithm can outperform the others in removing artifacts reliably without distorting neural signals.

ARTICLE INFO

Article history:
Received 19 August 2013
Received in revised form 22 January 2014
Accepted 23 January 2014

Keywords:
In vivo neural recording
Artifact characterization
Neural signal spectra
Wavelet transform

ABSTRACT

Background: *In vivo* neural recordings are often corrupted by different artifacts, especially in a less-constrained recording environment. Due to limited understanding of the artifacts appeared in the *in vivo* neural data, it is more challenging to identify artifacts from neural signal components compared with other applications. The objective of this work is to analyze artifact characteristics and to develop an algorithm for automatic artifact detection and removal without distorting the signals of interest.
New method: The proposed algorithm for artifact detection and removal is based on the stationary wavelet transform with selected frequency bands of neural signals. The selection of frequency bands is based on the spectrum characteristics of *in vivo* neural data. Further, to make the proposed algorithm robust under different recording conditions, a modified universal-threshold value is proposed.
Results: Extensive simulations have been performed to evaluate the performance of the proposed algorithm in terms of both amount of artifact removal and amount of distortion to neural signals. The quantitative results reveal that the algorithm is quite robust for different artifact types and artifact-to-signal ratio.
Comparison with existing methods: Both real and synthesized data have been used for testing the proposed algorithm in comparison with other artifact removal algorithms (e.g. ICA, wICA, wCCA, EMD-ICA, and EMD-CCA) found in the literature. Comparative testing results suggest that the proposed algorithm performs better than the available algorithms.
Conclusion: Our work is expected to be useful for future research on *in vivo* neural signal processing and eventually to develop a real-time neural interface for advanced neuroscience and behavioral experiments.

© 2014 Elsevier B.V. All rights reserved.

1. Introduction

Extracellularly recorded neural data from *in vivo* experiments provide higher spatio-temporal resolution and SNR compared with other non-invasive brain signal recordings; e.g. EEG, MEG, fMRI, etc. (Eichenbaum, 2001; Foffani and Moxon, 2003; Dayan and Abbott, 2005; Lytton, 2002; Mitra and Bokil, 2008; Buzsáki et al., 2012). While the recorded data can be corrupted by artifacts and interferences, especially under a less constrained recording protocol. Hence as a part of neural data preprocessing procedure, the detection and removal of artifacts without distorting the signals of interest play an important role. Compared with other applications, artifact detection and removal for *in vivo* neural recordings have the following application related challenges:

- **The signal characteristics:** Many other physiological signal recordings mostly contain narrow-band neural data (e.g. bandwidths of EEG, ECG, and EMG in general range from sub Hz to no more than a few hundred Hz); while *in vivo* neural recordings have a broad spectral band, i.e. from sub-1 Hz to several kHz. Thus,

* Corresponding author. Tel.: +65 93986197.
E-mail addresses: kafiul_islam@nus.edu.sg, kafiiut@gmail.com (M.K. Islam).

0165-0270/$ – see front matter © 2014 Elsevier B.V. All rights reserved.
http://dx.doi.org/10.1016/j.jneumeth.2014.01.027

spectral overlapping between artifacts and signals of interest for *in vivo* recordings is larger. Apart from the wide bandwidth, the presence of different signal components (i.e. Local Field Potentials (LFP), neural spikes, synaptic activities, etc.) and their highly non-stationary properties (Tomko and Crapper, 1974; Lewicki, 1998; Kaneko and Suzuki, 2007; Bar-Hillel and Spiro, 2005) compared with other recordings, make it more difficult for identifying artifacts.

- **The artifact characteristics:** When dealing with other physiological signals, often the appeared artifacts have certain stereotype waveforms or the artifact source itself can be recorded by a reference channel. This is not the case for *in vivo* neural recordings. In fact, as it will be discussed later, the diversity in artifact types, their properties and the way they appear in the recordings make it more challenging in separating them from neural signals.
- **Deficiency of available algorithms:** Many available algorithms for artifact detection and removal cannot be applied on *in vivo* recordings for the same purpose. For example, a most frequent method to detect and remove artifacts in EEG signals is based on blind source separation (BSS). One assumption of BSS is that the observations are linear mixing of the sources and the number of sources is equal or less than the number of observations. Another assumption is that the sources have to be either independent for ICA based methods (Flexer et al., 2005; Winkler et al., 2011; Delorme et al., 2007; Guerrero-Mosquera and Navia-Vazquez, 2012; Scott, 2011; Rong and Contreras-Vidal, 2006) or maximally uncorrelated for CCA based methods (Sweeney et al., 2013; Safieddine et al., 2012; Raghavendra and Dutt, 2011; Zhao and Qiu, 2011). However, the mentioned assumptions most often do not match with the *in vivo* neural recordings. For *in vivo* neural data, spiking activities from a same neuron mostly appear in one or few adjacent channels, where in the rest of the channels, those activities merge into the noise floor. Therefore, spikes cannot be separated as an independent source if BSS-based algorithm is applied. Different from artifacts in EEG, the artifacts found here are sometimes localized in a single channel, which suggests that the cross-channel analysis cannot be directly applied. Again there could be some correlation present between neural spikes and LFP (Buzsáki et al., 2012; Wang et al., 2006) which violets the assumption of BSS as mentioned. Although, there are available algorithms in the literature, e.g. wavelet-based (Molavi and Dumont, 2010; Castellanos and Makarov, 2006; Zima et al., 2012; Hsu et al., 2012) and EMD/HHT-based (Zhang et al., 2009; Wang et al., 2008) algorithms to remove such localized artifacts from individual single channel and they do not assume any independence/uncorrelation between sources unlike BSS. However, while applying for *in vivo* data, not only their performances are inadequate but also the computational burden can be heavy (e.g. EMD/HHT based algorithms) (Fonseca-Pinto, 2010).

In this paper, first of all, the characteristics of labeled artifacts appeared in *in vivo* neural recordings are analyzed and accordingly those artifacts are classified into four types. Subsequently, an artifact detection and removal algorithm is proposed. The algorithm relies on the spectrum characteristics of the neural signals (i.e. LFP and neural spikes) for artifact detection. It further applies stationary wavelet transform (SWT) to detect possible artifactual regions from the decomposed wavelet coefficients. Once artifacts have been detected, to restore neural signals, a modified version of the existing universal-threshold value is proposed, which makes the algorithm more robust.

In order to validate the proposed algorithm with quantitative measures, extensive simulations have been performed on both real and synthesized data.

The rest of this paper is organized as follows. Section 2 gives the problem description. Section 3 focuses on formulation and analysis.

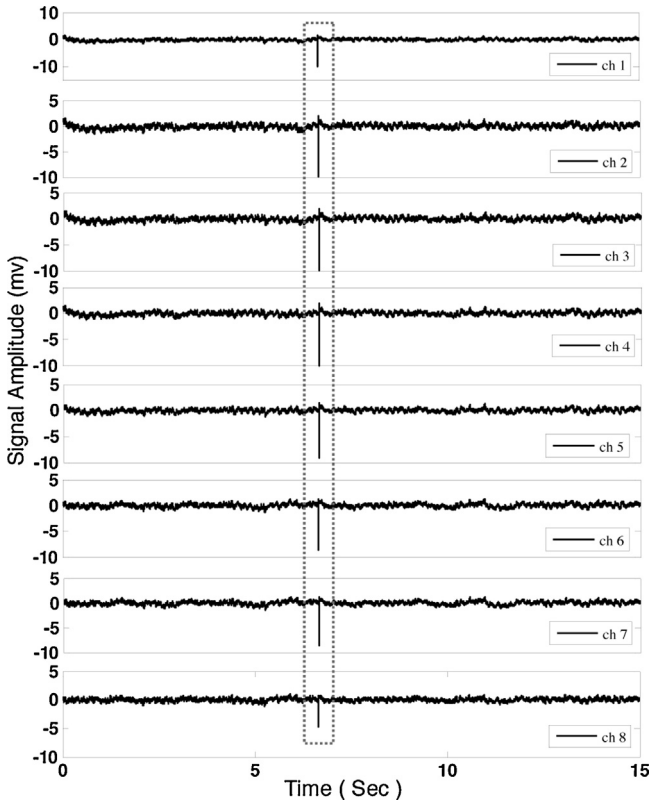


Fig. 1. Example of global artifacts appearing in all the recording channels at same temporal window. The data are recorded from the hippocampus of a rat.

In Section 4 comparative simulation results are presented. Section 5 provides discussions about the performance of the proposed algorithm. Section 6 gives concluding remarks.

2. Artifact characterization

In this section, the characterization of different artifacts, their sources and properties are presented. Such characterization efforts help to develop a better algorithm and generate synthesized neural database for performance assessment of the algorithm.

2.1. Artifact sources

Artifacts in a broad sense can be classified into two categories: *local* and *global*. Local artifacts are localized in space, i.e. appear only in a single recording channel while global artifacts can be seen across multiple channels of an electrode array. An example to illustrate global artifacts is shown in Fig. 1. The artifacts can also be classified into *external* and *internal* categories based on their origins (Savelainen, 2010, 2011). Internal artifacts arise from body activities, e.g. due to movements made by the subject itself, sudden changes of bioelectrical potentials, muscle activities, sudden chemical releases, etc. While external artifacts result from couplings with unwanted external interferences e.g. power line noise, sound/optical interferences, EM-interferences, etc. The artifacts may appear only once in the whole recording sequence, sometimes they can also appear in a regular/periodic manner. Examples of such artifacts are shown in Fig. 2.

2.2. Artifact templates

There are a number of factors and sources for artifacts, each could add different waveform signatures. After manual labeling,

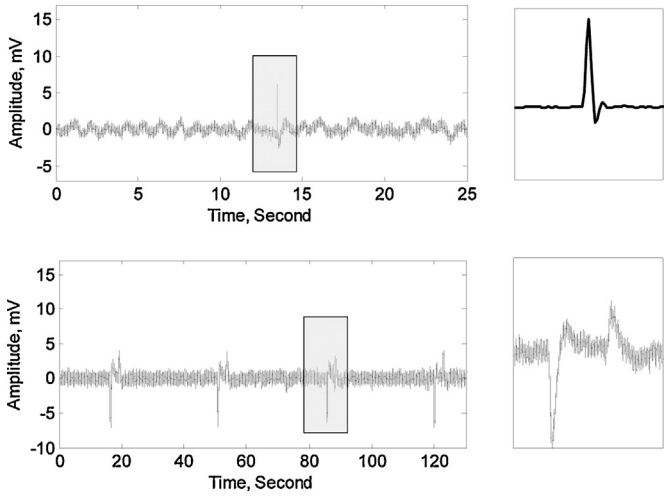


Fig. 2. Illustration of rarely appeared (top) and periodic (bottom) artifacts with zoom-in view on the right side. The appeared data have been recorded from the hippocampus of a rat.

the wide array of possible artifacts are characterized into four types based on different signatures, i.e. sharpness of edge, duration and waveform shape. The four types of artifacts are shown in Fig. 3 and described as follows:

Type-0: It has dominant power spectrum in low frequency region. They may appear as a single waveform or in a periodic fashion in recordings and over different channels. For example, this artifact can be generated from the muscle activities of the subject during movement.

Type-1: It is similar to step response, where there is an instantaneous large impulse whose effects are dampened over a period of time. Individual artifacts may have different widths and different decaying spectra with frequency. However, due to the sharp edge, there always exist localized high frequency features. The interconnect cable between the electrode and the pre-amplifier may work as antenna and picks-up some type-1 artifacts due to the subject's motion.

Type-2: Type-2 artifacts have been observed more frequently compared with both Type-0 and Type 1 artifacts. They usually have two fast ramp edges at two ends and can be modeled as the derivatives of the type-1 artifacts, which suggest that type-2 artifacts are another form of type-1 artifacts possibly generated from the same sources. The settling of electrodes may also produce such type of artifacts.

Type-3: Type-3 artifacts are often large (sometimes cause recording saturation) and narrow in width (less than 200 μs). They could appear both as individual waveforms and in a train, and tend to appear simultaneously over different channels. Different from neural spikes and local field potentials, they have a wide spectrum up to the low pass corner frequency set by recording electronics. This type of artifact may be generated from a sudden charge injection and discharging to the electrode/electronics.

Apart from the mentioned four types, there could be other types of artifact present as well, but these four types are supposed to represent/cover most of the artifact types. Because the way they have been classified (i.e. based on waveform shapes, appearance and/or frequency characteristics) is quite universal and almost any appeared artifact we found can be fallen in one of the four types. This paper deals with the mentioned four types of artifacts for quantitative evaluation of the proposed algorithm. However, it is discussed later that the algorithm does not depend on the artifact types rather it depends on the spectrum characteristics of the signal of interest. Therefore it can be applied to other types of artifacts (beyond these four types) as well.

3. Proposed algorithm

Let's assume $r(n)$ as the recorded neural data at discrete-time instant n and it can be expressed as:

$$r(n) = x(n) + a(n), \tag{1}$$

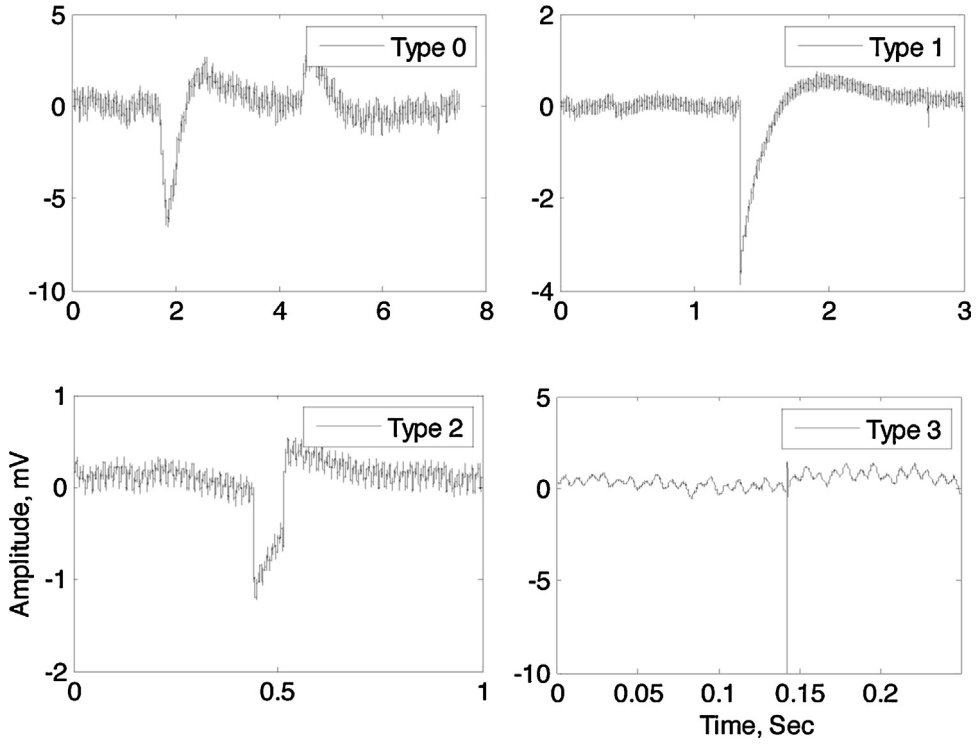


Fig. 3. Different types of artifact present at *in vivo* neural recordings from a rat hippocampus.

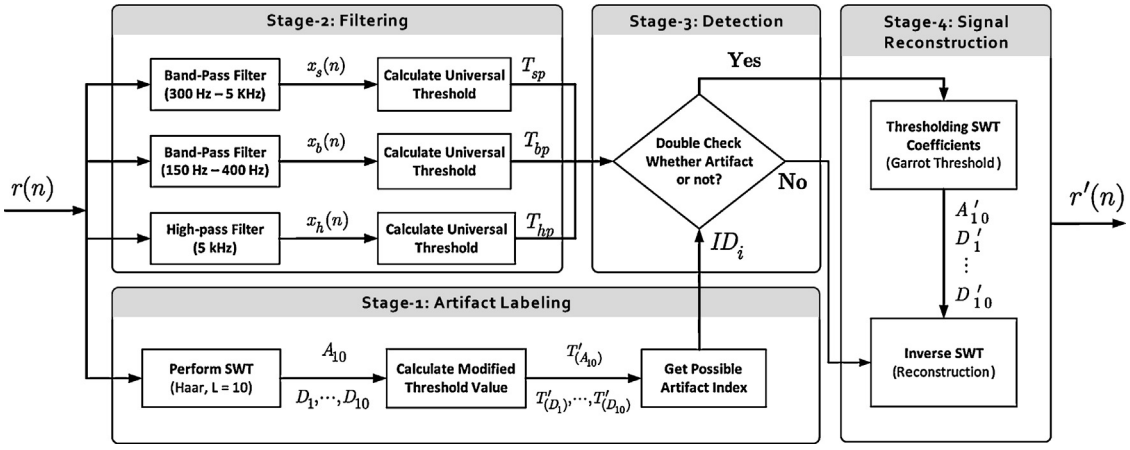


Fig. 4. Overview of the proposed algorithm.

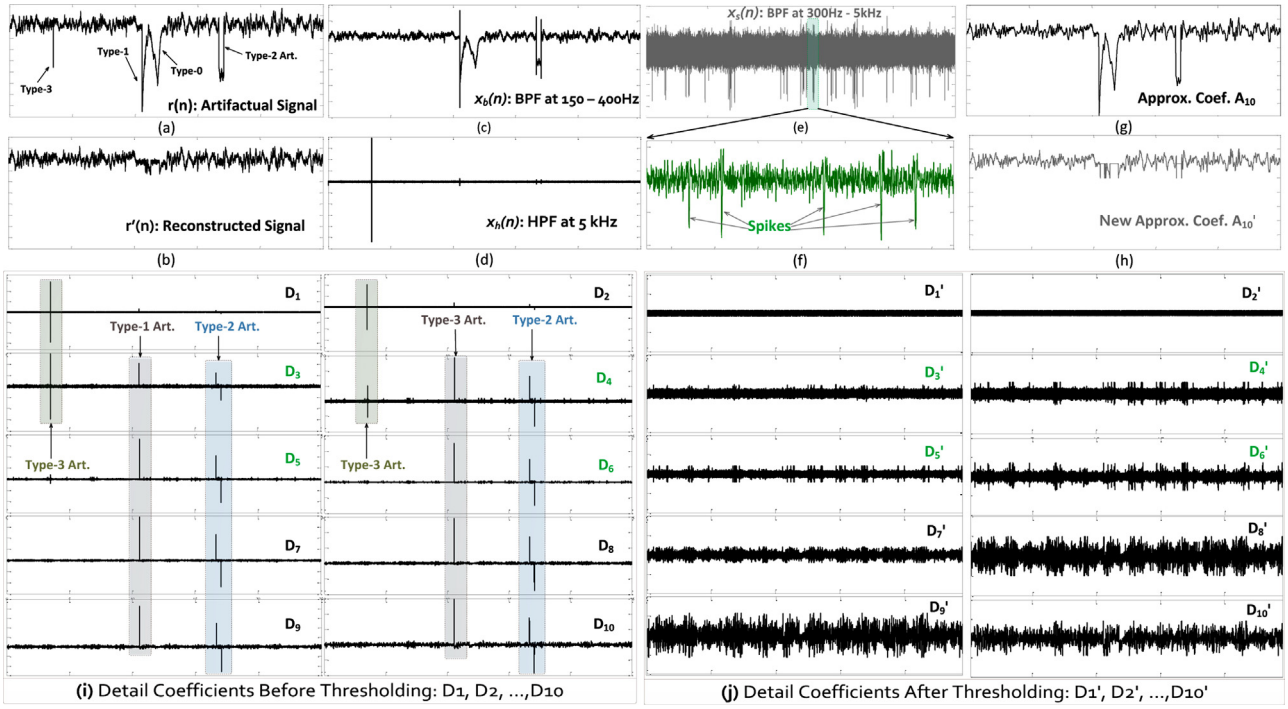


Fig. 5. An example of all the signals at different stages (as mentioned in the proposed algorithm flow in Fig. 4) in the same temporal domain is provided. A 10-level SWT decomposition is performed to an artifactual signal with Haar basis wavelet: (a) artifactual signal, $r(n)$; (b) reconstructed signal, $r'(n)$; (c) $x_s(n)$ obtained from band-pass filtering $r(n)$ at 300 Hz–5 kHz; (d) a zoom-in version of (c) showing few spikes; (e) $x_b(n)$ obtained from band-pass filtering r_n at 150 Hz–400 Hz; (f) $x_h(n)$ obtained from high-pass filtering $r(n)$ at 5 kHz; (g–h) the final approximate coefficient before and after thresholding respectively; and (i–j) the detail coefficients before and after thresholding, respectively.

where $x(n)$ and $a(n)$ are actual neural signals (i.e. spikes and field potentials) and artifacts respectively. The proposed artifact removal algorithm is composed of four stages including artifact labeling, verification, detection, and reconstruction, as shown in Fig. 4. In the following each stage of the proposed block diagram is described in more detail.

3.1. Artifact labeling

Wavelet transform has been chosen to assist labeling artifacts. The reason is that it is suitable for non-stationary signal analysis (e.g. neural signals) and is a powerful tool to detect abrupt changes or localized events mostly due to artifacts (Mallat, 2008). Among different wavelet transforms, the discrete wavelet transform (DWT) is the simplest one in terms of computational complexity.[1] However, the problem of DWT is that it is not translation invariant. Therefore small shifts in a signal can cause large changes in the wavelet coefficients and large variations in the distribution of energy in the different wavelet scales (Molla et al., 2012; Coifman and Donoho, 1995). Hence, denoising with DWT often introduces artifacts in the signal near discontinuities during signal reconstruction (Safieddine et al., 2012). One solution is to use stationary wavelet transform (SWT) which is translation invariant, as there is no down sampling of data involved in the algorithm

[1] The computational complexity of DWT is $\mathcal{O}(N)$ while the computational complexity of SWT is $\mathcal{O}(NL)$ (Beylkin, 1992) using fast transform (Moen, 2007). Here L is the number of decomposition level and N is the signal length.

Table 1
The frequency bands of the respective SWT coefficients and corresponding signal components for a 10-level decomposition. Here two typical sampling frequencies for extracellular neural recordings are considered (i.e. 40 kHz and 30 kHz) and the maximum recording bandwidth is assumed to be half of the sampling frequency.

SWT Coef. (L=10)	Fs (kHz)	D_1	D_2	D_3	D_4	D_5	D_6	D_7	D_8	D_9	D_{10}	A_{10}
Freq. Band	40	10 – 20 kHz	5 – 10 kHz	2.5 – 5 kHz	1.25 - 2.5 kHz	625 Hz – 1.25 kHz	312 - 625 Hz	156 - 312 Hz	78 - 156 Hz	39-78 Hz	19.5-39 Hz	0 - 19.5 Hz
	30	7.5 – 15 kHz	3.75 – 7.5 kHz	1.875 – 3.75 kHz	0.937 - 1.88 kHz	469 Hz – 937.5 Hz	234 - 469 Hz	117 - 234 Hz	58.5 - 117 Hz	29 - 58.5 Hz	14.5 - 29 Hz	0 - 14.5 Hz
Signal Component				← Neural Spike →					← LFP →			

(Molla et al., 2012; Coifman and Donoho, 1995; Safieddine et al., 2012).

3.1.1. SWT decomposition

The SWT is performed on the artifactual signal $r(n)$ at level $L = 10$ with Haar as basis wavelet function.[2] Thus, two types of coefficients are generated: approximate and detail coefficients that contain low and high frequency information respectively as shown in Fig. 5. The generated wavelet coefficients at different levels denote the correlation coefficients between artifactual signal and the wavelet function. The artifactual events will have larger coefficient values if they have higher correlation with the wavelet function while smaller coefficients will be generated corresponding to the actual neural activities. In order to perform thresholding, the selected coefficients are the final approximate coefficient, A_{10} and all the detail coefficients i.e. $D_1, \ldots, D_{10}$. A_{10} consists of all low frequency components (from 0 Hz to 19.5 Hz), such as electrode offset, some part of information from LFPs, neuron noise and artifacts (e.g. type-0, type-1 and type-2). While, $D_1, \ldots, D_{10}$ contain the high frequency information such as neural spikes, type-3 artifacts and sharp edges from artifacts of type-1 or type-2. A plot is shown in Table 1 to illustrate the frequency bands of different level of coefficients and the corresponding neural signal bands. It reveals that even in the decomposed coefficients, the artifacts can overlap with the neural signals of interest. Therefore the threshold is chosen carefully in order to detect and suppress possible artifactual activities from the decomposed coefficients.

3.1.2. Threshold calculation

The next step is to calculate a threshold value to detect the artifacts in the wavelet domain. The choice of threshold value will decide both the amount of artifact suppression and the amount of distortion to the neural signal at the same time. One possible solution is to use the universal threshold proposed by (Safieddine et al., 2012) which is given as follows:

$$T_j = \alpha_j \sqrt{2 \ln N}, \tag{2}$$

where N is the signal length and α_j is the estimated noise variance for W_j which is usually calculated by following formula (Safieddine et al., 2012)

$$\alpha_j = \frac{\text{median}(|W_j|)}{0.6745}. \tag{3}$$

In (3) W_j is the wavelet coefficients at the jth decomposition level ($W_j = A_j$ for approximation coefficient and, $W_j = D_j$ for detail coefficient). Here, $|\cdot|$ denotes the absolute value of elements in W_j. The constant denominator results in an unbiased estimate assuming the data are normally distributed (Gao, 1998). However, this particular threshold is fixed for each W_j and not optimal most of the time. By extensive testings, it has been found that this threshold is not suitable for our application as it may produce serious distortion to neural signals. Particularly for wavelet coefficients those contain components from spikes or when the neural recording has severe large artifacts such that the data distribution violates from the typical Gaussian fitting (a large tail in the histogram as shown in Fig. 6).[3] Hence it is proposed to include an extra parameter k to the original universal threshold formula in a following way and the resultant threshold modifies to

$$T'_j = k\alpha_j \sqrt{2 \ln N}, \tag{4}$$

where $k = \{k_A, k_D\}$, $0 < k_A < 1$, $1 < k_D < 5$, which comes from the empirical observations (see Appendix A). More precisely, $k = k_A$ is selected for thresholding approximate coefficient at final level, here it is A_{10} and select $k = k_D$ to threshold all the detail coefficients (D_j, $j = 1, 2, \ldots, 10$).

The tuning of parameter k_A depends on the data distribution as shown in Fig. 6. Since A_{10} contains both the LFP and some low-frequency artifacts, so when the histogram of the data has large deviation from the standard deviation (large tail on the histogram on either one side or both), it is more likely due to presence of artifacts. Therefore a value less than 1 is chosen for k_A and if there is no such unusual tail present, then $k_A = 1$ is chosen that makes

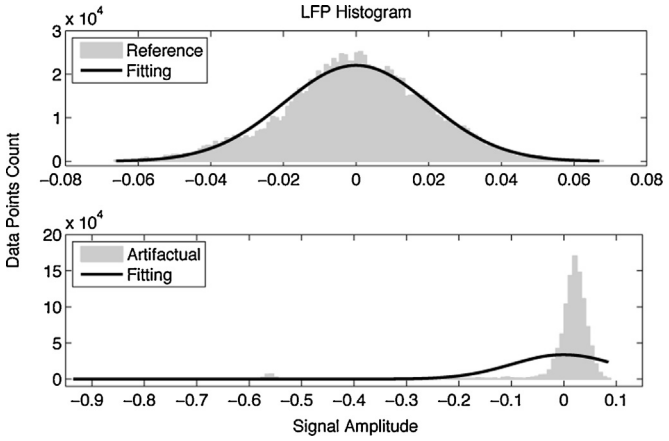


Fig. 6. Comparison in amplitude histogram of LFP for signal without (top) and with (bottom) artifacts. Gaussian fitting is shown in black.

[2] A majority of motion artifacts appear in the form of abrupt changes in the amplitude of the signal. Therefore, Haar is used as basis wavelet since due to its waveform shape, it can possibly detect and localize such artifactual events and they appear with relatively high amplitudes in the decomposed coefficients. The choice of level-10 decomposition is done empirically by considering two facts: (i) the no. of signal components present in the raw recordings and (ii) the trade-off between latency/storage and amount of detail information extraction. Less than level-10 would give less detail information and more than level-10 would consume unnecessary time and storage.

[3] The LFP distribution of an artifact-free reference data has significant fluctuations due to non-stationary property but has a shape almost similar to that of Gaussian when curve fitting is done. While the LFP distribution of an artifactual data fails to fit anywhere near to Gaussian because of its large tail at one of the sides as shown in Fig. 6.

the threshold exactly same as the original universal threshold, i.e. $T'_i = T_1$. The criterion for the choice of k_A is given below:

$$k_A = \begin{cases} 1 & \text{if } \max(|A_{10}|) > m \times sd(A_{10}), \\ 0 \le k_A < 1 & \text{otherwise}, \end{cases} \quad (5)$$

where *sd* denotes the standard deviation of A_{10}. The value of m is based on the parameter tuning and can be obtained from some initial several seconds of incoming raw *in vivo* data samples to update the threshold value. From the empirical studies, the value of m is found as minimum of 5, i.e. $5 < m < \infty$ (see Appendix A).

In order to decide the value of k_D, power spectra of all detail coefficients are studied and it is found that coefficients at level 3, 4, 5 and 6, i.e. D_3, D_4, D_5 and D_6 have highest power around the neural spikes' spectra and hence these three level contains spike information along with artifacts. Therefore it is chosen to put more weight ($k_D > 1$) on these coefficients and less on the rest of the level of coefficients (i.e. D_1, D_2, D_3, D_7, D_8, D_9 and D_{10}) as follows:

$$k_D = \begin{cases} 1 < k_i \le 5 & i = 3, \quad 4, \quad 5 \quad \text{and } 6, \\ 1 & \text{otherwise}, \end{cases} \quad (6)$$

where i denotes the detail decomposition level and the constant parameter k_D is chosen from the spike data histogram. The spikes present in neural data with very large amplitudes influence the selection of k_D towards higher value while if the spike amplitude is normal, then from empirical studies it is found that the value of k_D to be 2–3.

3.2. Filtering

Once the time indices are obtained from the decomposed coefficients after applying modified threshold function, T'_i; it is required to double check possible artifactual segments to separate artifacts from signals of interest, especially from spikes. The use of filtering is inspired from the spectrum characteristics of neural signal components: LFP and spikes. Although the spectral band of *in vivo* recordings has a wide spectrum, there are two prospective bands, i.e. 150–400 Hz and >5 kHz, where both LFP power and spike power are relatively low (Islam et al., 2012). Thus, band pass and high pass filtering are performed at 150–400 Hz and 5 kHz, respectively, for artifact detection. It is assumed here that the recording do not contain ripple band oscillations, which appears around 100–300 Hz, is ignored (Molle et al., 2006).

In order to detect spikes, the raw data is usually band-pass filtered from 300 Hz to 5 kHz (Belitski et al., 2008). Denoted by $x_b(n)$, $x_h(n)$ and $x_s(n)$ as the band-pass filtered, high-pass filtered and spike signals respectively and their corresponding universal threshold values are calculated by:

$$T_{bp,hp,sp} = \left(\frac{\text{median}(|x_{b,h,s}|)}{0.6745} \right) \sqrt{2 \ln N}, \quad (7)$$

These threshold values T_{bp}, T_{hp} and T_{sp} with the time indices of artifactual segments (provided by artifact labeling stage 3.1) are used to make the decision of whether artifacts or signals (stage 2 from Fig. 4).

3.3. Detection

Denote ID_i the time index for artifactual segment at decomposition level i found from the earlier stage, the condition for separation of artifact from neural signals is given by the following pseudo code:

Separation of artifacts from signals

```
If (|x_b(ID_i)| < T_bp) or (|x_h(ID_i)| < T_hp)
  If (|x_s(ID_i)| > T_sp)
    ID_i is not artifact index
  else
    ID_i is artifact index
  end
else
  ID_i is artifact index
end
```

3.4. Signal reconstruction

In the final stage, in order to reconstruct the signal, at first the coefficients are thresholded once it is confirmed as artifacts from stage-3. Thus a new set of coefficients, i.e. A'_{10}, and $D'_1, \ldots, D'_{10}$ are generated. Finally, inverse stationary wavelet transform is applied to the new coefficients to restore artifact-reduced neural signals.

The choice of threshold function is very important, as it influences the amount of attenuation to the SWT coefficients. A most popular thresholding function is hard threshold that has a discontinuity which may produce large variance to the reconstructed signal or in other words, output estimate is very sensitive to small changes in the input data (Gao, 1998). On the other hand, there is soft threshold function that is continuous but has larger bias in the estimated signal which results in larger errors. In order to overcome the disadvantages of these two threshold functions, the non-negative garrote shrinkage function is proposed in (Gao, 1998) which is a nice trade-off between hard and soft threshold function and is given by:

$$\delta_{G_i} = \begin{cases} 0 & |x| \le T'_i \\ x - \dfrac{T'^2_i}{x} & |x| > T'_i. \end{cases} \quad (8)$$

where δ_{G_i} is the garrote threshold function at each decomposition level of i. This function is less sensitive to input change, lower bias and more importantly continuous. Therefore garrote threshold function is chosen for our application.

4. Experiments

To validate the proposed algorithm, extensive testings have been performed on both real and synthesized data to facilitate both qualitative and quantitative measurements and compared with other algorithms in the literature. The data recording protocol is described below:

Neural recording data from in vivo preparations are provided by Edward Keefer at Plexon Inc./University of Texas Southwest Medical Institute and Victor Pikov at Huntington Medical Research Institute. For Keefer's data, the protocols are similar to (Keefer et al., 2008; Yang et al., 2009), where the subjects (rats) have been anesthetized for acute experiments. CNT electrodes, microwire, and electrode array have been used in experiments and connected to Plexon OmniPlex neural data acquisition system. For Pikov's data: the 16-channel electrode arrays with a nominal geometric area of exposed electrode tips were purchased from Blackrock Microsystems. The array was chronically implanted in the sensorimotor cortex and connected to a percutaneous connector mounted in the animal's (monkey) head. The experiment protocols are in accordance with the Institutional Animal Care and in compliance with the United States Department of Agriculture (USDA) Animal Welfare Act. We have been authorized by Edward Keefer and Victor Pikov to utilize the recorded data for research and publication.

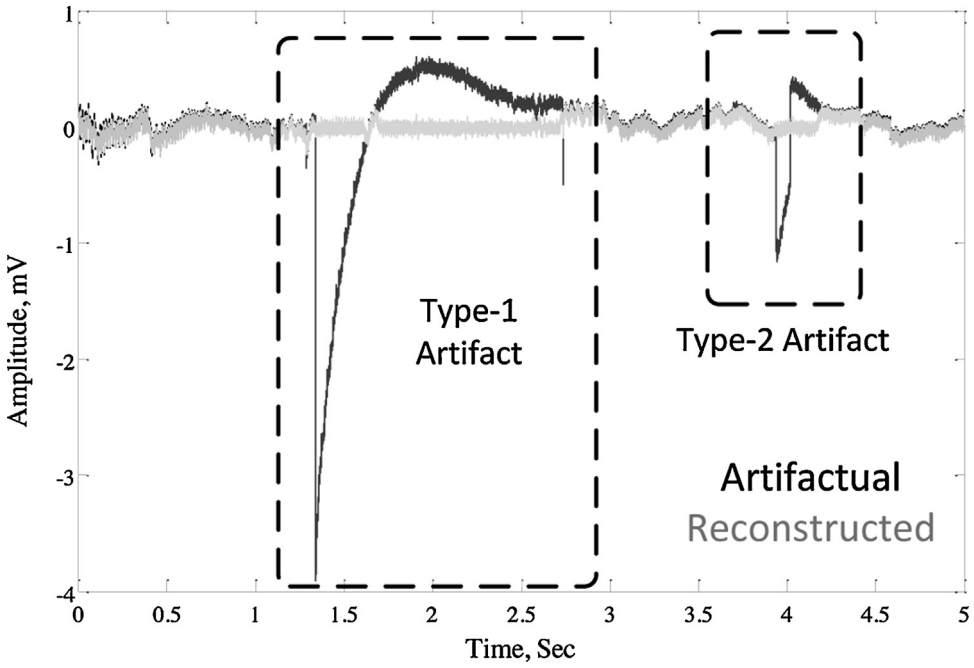


Fig. 7. Artifact removal algorithm applied to a raw *in vivo* data recorded from the hippocampus of a rat. The plot is the time course data where both type-1 and type-2 artifacts are present.

Synthesized data are prepared from *in vivo* recordings. Data segments without artifacts are used as ground truth data. Labeled artifacts by a domain expert are used as artifact templates. Individual artifacts under different templates are then simulated with different amplitudes, widths and durations and finally superimposed onto the ground truth data for quantitative assessment of algorithm performance.

4.1. Experiment on real data

Initially the proposed algorithm is tested on real *in vivo* data sequences contaminated with artifacts. Then both the data sequences before and after artifact removal are plotted in the same trace of time domain (as shown in Fig. 7) to observe whether it has removed the artifact or not. The local field potentials and spikes

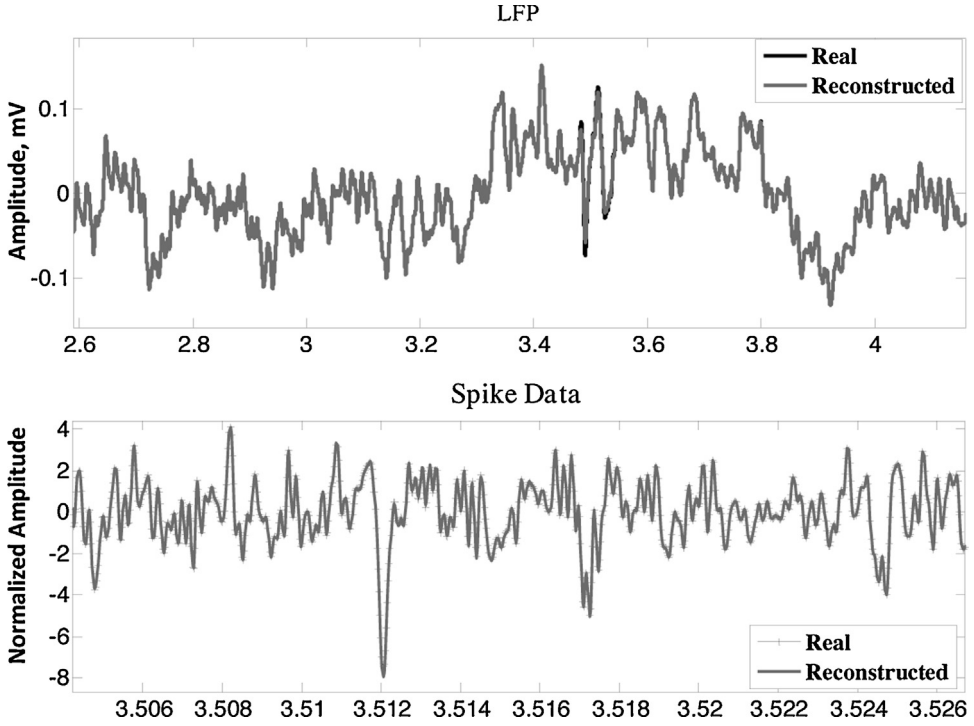


Fig. 8. A Comparison in field potentials and spike data when there are no visually detectable artifacts (a small data segment from Fig. 7 after low-pass filtering at 200 Hz and band-pass filtering at 300 Hz–5 kHz are performed to get LFP and spike data, respectively). The proposed algorithm nearly perfect reconstructs the original data when there is no artifact present.

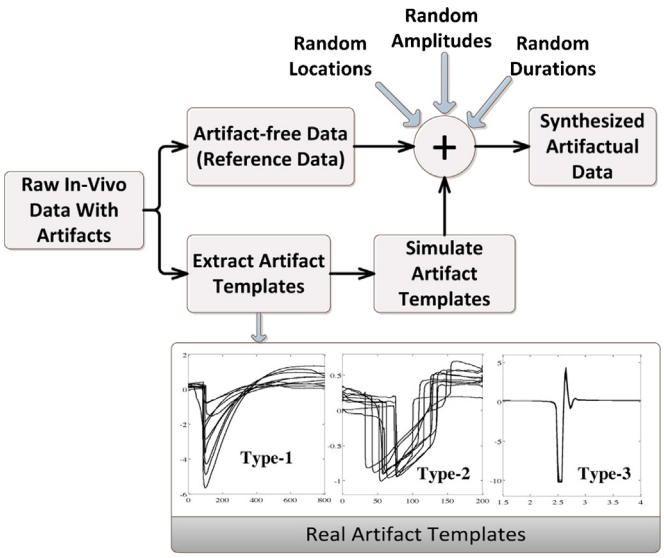


Fig. 9. Illustration of the synthesis process to generate artifactual data.

are also plotted for both data sequences to observe qualitatively (shown in Fig. 8) how much distortion it brings when there is no presence of visually detectable artifacts.

4.2. Experiment on synthesized data

Different artifacts have been manually identified and extracted (neural data segments contaminated with obvious visually detected artifacts) from real *in vivo* data and categorized each into one of the mentioned four types, i.e. type-0, type-1, type-2 and type-3. Based on these extracted templates, similar artifact templates are simulated with different amplitudes and durations. An *in vivo* neural data sequence of 100 s duration is chosen which does not contain any visually detectable artifacts and termed it as *reference signal*. Then the simulated artifacts are linearly added to the reference signal in different random positions with different amplitudes, edge widths and durations to form a data sequence that is contaminated with artifacts, it is referred to *artifactual signal*. The data synthesis process is illustrated in Fig. 9. Finally the proposed artifact removal technique is applied on the artifactual signal and the resultant data sequence is termed as *reconstructed signal*. An example of artifact removal is shown in Fig. 10. As mentioned that the proposed method is applied to the artifactual data to get the artifact-reduced reconstructed data which is more similar to the reference data.

4.2.1. Efficiency metrics

The measurement for quantitative evaluation of the algorithm is mainly two types: one is to measure how much artifact has been removed and the other one is to measure how much distortion it brings into the signal of interest. The first type of measurement includes two metrics: the amount of artifact reduction in percentage, λ as mentioned in (Sweeney et al., 2013) and the amount of increase in signal to noise ratio (SNR), ΔSNR for different artifact amplitude or artifact SNR (SNR_{Art}). The second type of measurement is to quantify the amount of signal distortion which includes: spectral distortion, P_{dis} as defined in (Yong et al., 2012) and root mean square error, *RMSE*. The former one refers to distortion in frequency domain and the later one measures the distortion in time domain. Also the efficacy of the algorithm is evaluated in terms of ROC (Receiver Operating Characteristics) plot for spike detection before and after artifact removal in comparison with the reference signal. The calculations of the mentioned metrics are discussed

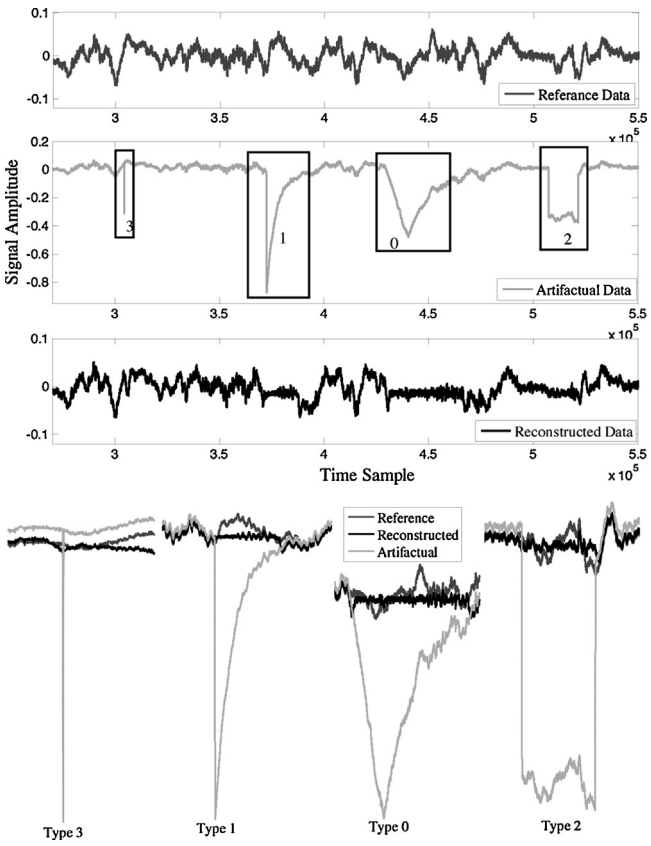


Fig. 10. Artifact removal example by the proposed method where the artifactual signal (synthesized) is corrupted by all four types of artifact. The top plot shows the three different time course signals of reference, artifactual and reconstructed. The bottom plot is the zoom-in version of the previous plot highlighted on the artifact-affected regions.

below. Please note that the following calculations can only be performed on synthesized data. Assuming $x(n)$, $r(n)$ and $r'(n)$ are the discrete time signals of length N representing reference, artifactual and reconstructed signal respectively. If the error signal before and after artifact removal are e_1 and e_2 respectively and calculated as follows:

$$e_1(n) = r(n) - x(n), \tag{9}$$

$$e_2(n) = r\prime(n) - x(n). \tag{10}$$

- **λ**: The reduction in artifact, λ is calculated using the following formula (Sweeney et al., 2013):

$$\lambda = 100\left(1 - \frac{R_{ref} - R_{rec}}{R_{ref} - R_{art}}\right), \tag{11}$$

  Here, R_{ref} denotes the auto-correlation of the reference signal at time lag 1, R_{art} and R_{rec} are the cross-correlation between reference signal with artifactual and reconstructed signal, respectively.
- **ΔSNR**: Assuming the signals have zero mean, the ΔSNR is the difference in SNR before and after artifact removal is given by the following formula (Sweeney et al., 2013):

$$\Delta\text{SNR} = 10\log_{10}\left(\frac{\sigma^2_{ref}}{\sigma^2_{e_1}}\right) - 10\log_{10}\left(\frac{\sigma^2_{ref}}{\sigma^2_{e_2}}\right), \tag{12}$$

  where σ^2_{ref}, $\sigma^2_{e_1}$ and $\sigma^2_{e_2}$ be the variance of reference signal, error signal before and after artifact removal, respectively.

- **RMSE**: The root mean square error, *RMSE* is calculated as follows:

$$RMSE = \sqrt{\frac{1}{N}\sum_{n=1}^{N}[e_2(n)]^2}. \quad (13)$$

- $\mathbf{P}_{dis}$: Denote $PSD_{Ref}(f)$, $PSD_{Art}(f)$ and $PSD_{Recon}(f)$ the power spectral densities of reference signal, artifactual signal and reconstructed signal respectively, the spectral distortion P_{dis} is calculated as follows:

$$P_{dis} = \frac{\sum (PSD_{Recon}(f))^2}{\sum (PSD_{Ref}(f))^2}. \quad (14)$$

- $\mathbf{SNR}_{Art}$: Artifact SNR is calculated considering artifact as signal and reference neural signal as noise using the following formula:

$$\mathrm{SNR}_{Art} = 10\log_{10}\left(\frac{\sigma_{e_1}^2}{\sigma_{ref}^2}\right). \quad (15)$$

- $\mathbf{\Delta T}_{Art}$: It denotes the artifact duration out of total data length in percentage and calculated as follows:

$$\Delta \mathrm{T_{Art}}(\%) = \frac{T_{Art}}{T_{Total}} \times 100, \quad (16)$$

where T_{Art} and T_{Total} are the time duration of artifact and whole data sequence, respectively.

- **ROC curve**: In order to evaluate the spike detection accuracy of a ROC curve, the simple amplitude threshold based detection method (Harrison, 2003; Yang, 1988; Chandra, 1997; Snider, 1998) is used and compared with the reference signal. The true positive rate (TPR) and false positive rate (FPR) are calculated by following equations:

$$\mathrm{TPR} = \frac{TP}{TP + FN}, \quad (17)$$

$$\mathrm{FPR} = \frac{FP}{FP + TN}, \quad (18)$$

where *TP*, *TN*, *FP* and *FN* are the number of spikes detected as true positive, true negative, false positive and false negative, respectively.

- **ΔFPR(%) and ΔTPR(%)**: If FPR_{bef} and FPR_{aft} are the false positive rate before after artifact removal while TPR_{bef} and TPR_{aft} are the true positive rate before after artifact removal respectively, then the improvement in FPR, ΔFPR(%) and in TPR, ΔTPR(%) are given by:

$$\Delta \mathrm{FPR}(\%) = \frac{\mathrm{FPR}_{bef} - \mathrm{FPR}_{aft}}{\mathrm{FPR}_{bef}} \times 100, \quad (19)$$

$$\Delta \mathrm{TPR}(\%) = \frac{\mathrm{TPR}_{aft} - \mathrm{TPR}_{bef}}{\mathrm{TPR}_{bef}} \times 100, \quad (20)$$

5. Results and discussion

5.1. Effect of filtering

In Fig. 11, an example of a 'Receiver Operation Characteristic' (ROC) curve for spike detection is plotted where the improvement due to the inclusion of filtering along with SWT in comparison with only SWT is obvious. As mentioned in Section 3.2, the reason for inclusion of filtering (i.e. HPF at 5 kHz and BPF at 150–400 Hz) is to preserve the spike information (i.e. spike time and shape both) and thus able to distinguish from artifacts. The decomposed wavelet coefficients are also thresholded adaptively and selectively in order to preserve the spikes according to Section 3.4. The data corrupted with very large amplitude artifacts, especially type-3; result in a larger number of false negatives (FN). Since the presence of such

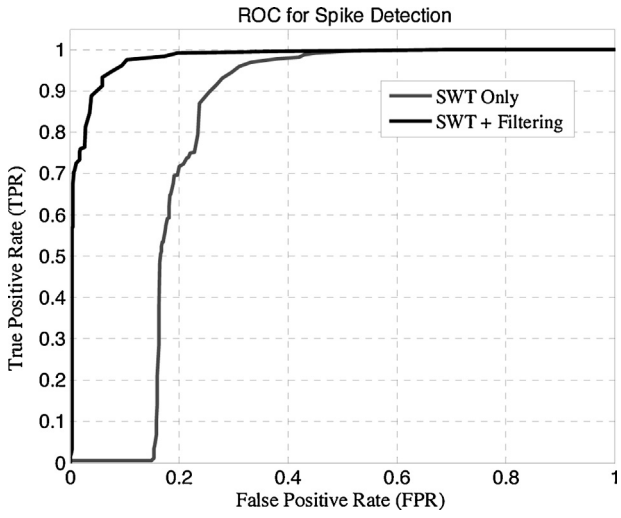


Fig. 11. ROC curve evaluating neural spike detection accuracy to illustrate the effect of filtering in combination with SWT compared with only SWT.

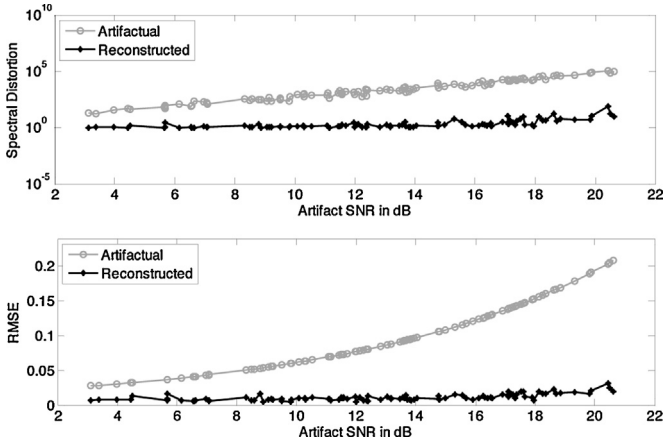


Fig. 12. Amount of distortion to neural signal in terms of spectral distortion (top) and root mean square error, RMSE (bottom) before and after artifact removal for different artifact SNR.

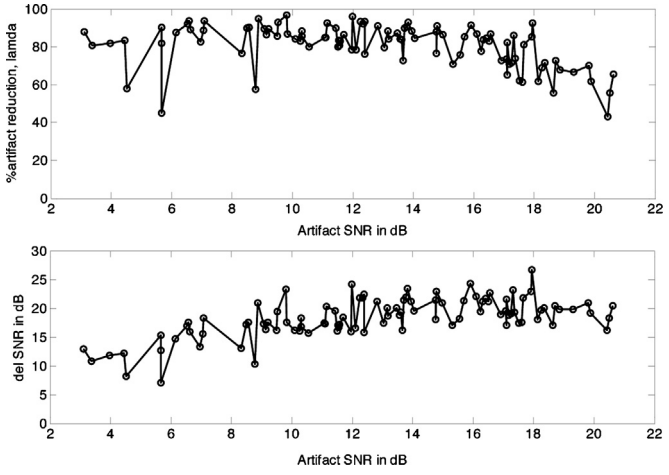


Fig. 13. Amount of artifact removal in terms of Lambda, λ (top) and amount of SNR improvement, ΔSNR (bottom) for different artifact SNR after artifact removal is performed.

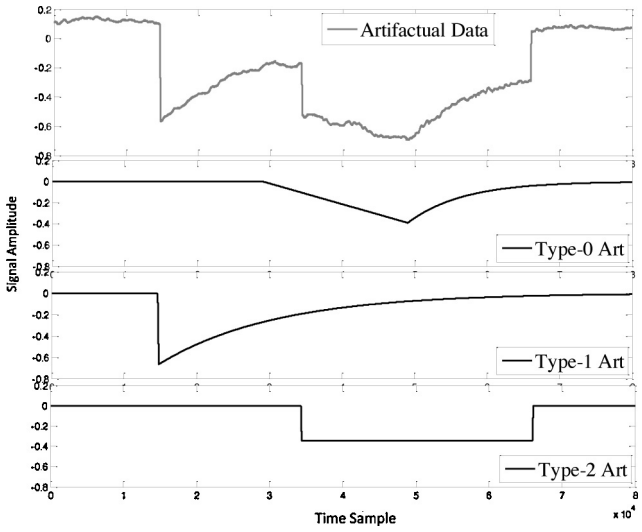


Fig. 14. An example of overlapping of different artifact types in temporal domain in a synthesized artifactual data.

artifacts increases the data RMS (root mean square) and so does the detection threshold which eventually misses some of the true spikes due to their relatively lower amplitude compared to artifacts. On the other hand, the presence of type-3 artifacts and edges of type-1, type-2 artifacts result in false positives (FP) during spike detection.

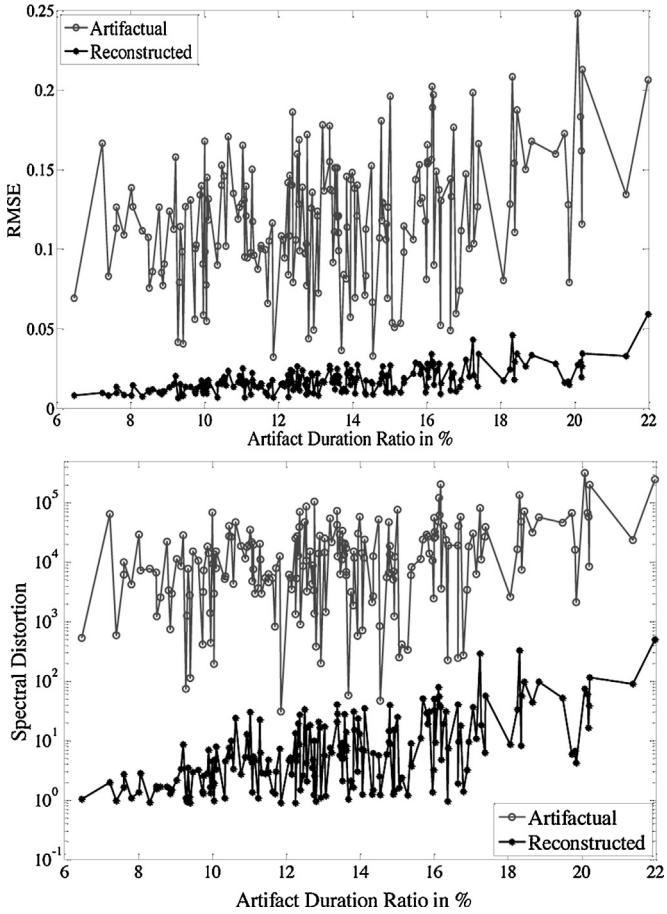


Fig. 15. Amount of distortion to neural signal in terms of root mean square error, RMSE (top) and spectral distortion (bottom) before and after artifact removal for different artifact duration.

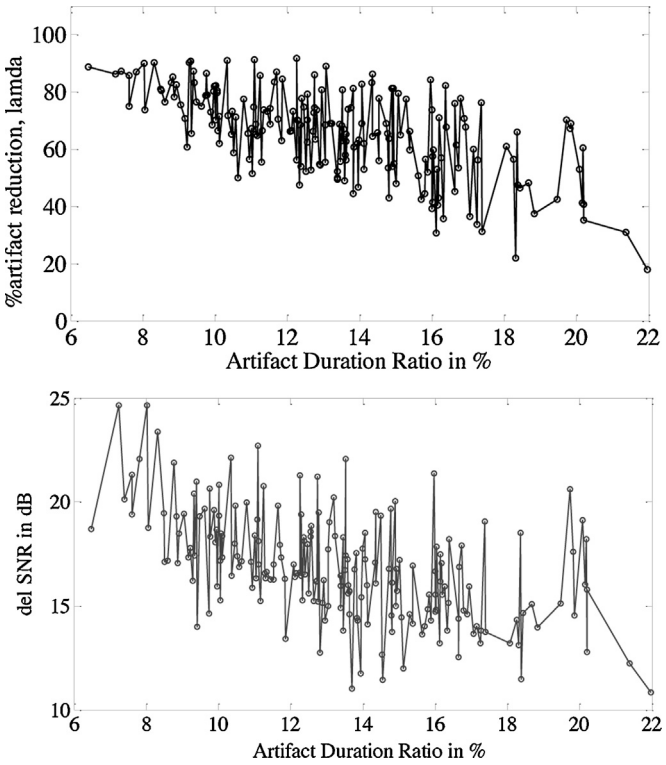


Fig. 16. Amount of artifact removal in terms of Lambda, λ (top) and amount of SNR improvement, ΔSNR (bottom) for different artifact duration after artifact removal is performed.

5.2. Quantitative evaluation

The simulation for quantitative evaluation is performed for 100 iterations where each iteration has random number of artifacts (ranging from 4 to 10) with random time durations (ranging from 200 μs to 1 s) placed in random locations on top of the reference signal. The artifact removal performance has been evaluated at different artifact SNR, SNR_{Art} in order to observe the effects of artifact strength on the removal efficacy. Fig. 12 shows the spectral distortion with respect to different artifact SNR for the data before and after artifact removal. The spectral distortion for artifactual data increases almost linearly in log scale as the artifact strength increase while the distortion for reconstructed data is somewhat constant up to 15 dB SNR of artifact and increases very slowly as artifact SNR further increases. The similar case can be seen for RMSE (which is temporal distortion) that the increase is logarithmically for artifactual data as artifact SNR increases while on the other hand, for reconstructed data it is more or less constant over the entire range of artifact SNR. It is worth to mention that in both cases, the improvement in terms of reduction in signal distortion is very impressive after artifact removal process is performed.

By observing the performance of artifact removal in Fig. 13, it can be seen that, on average, approximately 80% of artifacts are removed over the wide range of artifact SNR. The reason of no particular trend in the graph may be due to the random positions of artifacts and their temporal overlapping as shown in Fig. 14. In some iterations, in spite of artifact SNR being large, different types of artifact may overlap in temporal domain which slightly reduces the efficacy of the removal method. The increase in signal SNR with different artifact SNR follows somewhat linear trend with a positive offset probably due to the overcorrection in the artifact regions in some cases.

The mentioned four performance metrics are also evaluated with respect to the percentage of artifact duration out of the whole

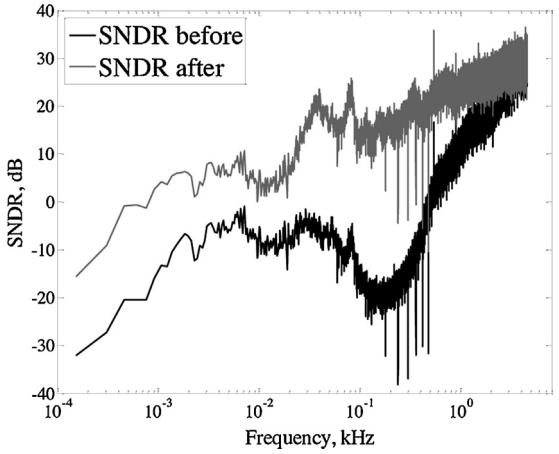


Fig. 17. SNDR comparison between signals before (artifactual) and after (reconstructed) artifact removal. The SNDR values are averaged over 200 interactions.

data segment duration in temporal domain in order to observe the algorithm's response or sensitivity to the amount of artifact duration. It is expected that, the higher the duration of artifacts (i.e. higher temporal overlapping with signals) present in a data sequence, the more difficult to remove them without distorting the signal of interest. The relevant plots are shown in Fig. 15 and Fig. 16 where the distortions in both temporal and spectral domain are plotted respectively with respect to the percentage artifact duration for data before and after artifact removal.

Fig. 17 shows the average signal-to-noise-and-distortion ratio (*SNDR*) over the frequency band of neural signals for both artifactual and reconstructed data to illustrate the improvement in *SNDR*.

5.3. Qualitative analysis

The proposed algorithm is also applied to the real *in vivo* datasets which contain obvious artifacts. The reconstructed data after application of the removal process is plotted in time domain to compare with the real data qualitatively as previously shown in Fig. 7.

5.4. Comparison with other methods

Table 2 summarizes the comparison between the proposed method and other available methods used for artifact removal in physiological signals (e.g. EEG, fMRI, MEG, ECG, etc.). The recent review paper (Sweeney et al., 2012) reports the techniques used so far in artifact removal and made an extensive comparison between them. Among these techniques, the proposed algorithm is compared with wICA, wCCA, ICA, EMD-ICA and EMD-CCA (the methods are described in Fig. 18). From Table 2, it is evident that the proposed method outperforms all of these five methods most of the time in removal of the artifacts tested in this paper. The possible reasons are intuitive, ICA and CCA usually perform better for global artifacts and fail to identify the local ones (Islam et al., 2012). So even wICA and wCCA work satisfactory with EEG artifacts where at least few channels capture the global artifactual events, they fail in identifying the *in vivo* artifacts which could also be local. The distortions brought by these algorithms are also higher compared with the proposed method. Since both wICA and wCCA are based on DWT, hence

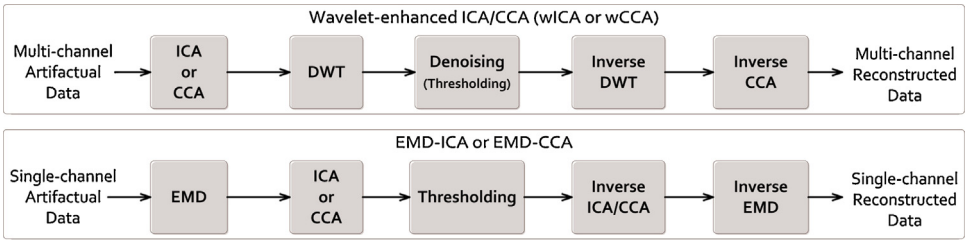


Fig. 18. Process flow of other methods used for comparison in this paper: wICA, wCCA, EMD-ICA and EMD-CCA.

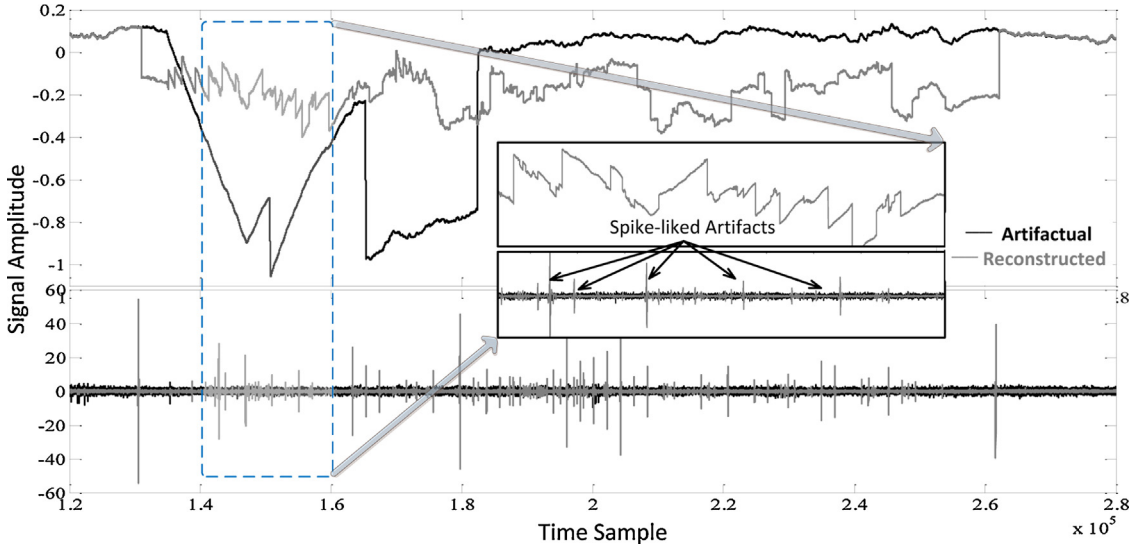


Fig. 19. Example of spike-liked artifacts produced after wICA algorithm is applied on artifactual signal. The upper trace is the superimposed representation of reconstructed signal on artifactual signal and the lower trace is the spike data after and before artifact removal derived from the upper-trace data after BPF is performed from 300 Hz to 5 kHz.

Table 2
Quantitative comparison of proposed method with other methods on artifact removal for different artifact SNR (SNR_{Art}).

SNR_{Art} (dB)	Proposed	wICA	wCCA	ICA	EMD-ICA	EMD-CCA
Artifact reduction, λ (ideal value = 100)						
5	58	30	45.5	46.45	−1.82	9
10	85	8	40	33.1	−3.8	3.4
15	90	−1	37	38.2	22.25	1.3
20	60	5	29	25.1	26	16
25	18.5	−3.5	8.85	17.25	−5.5	4.2
Signal SNR improvement, ΔSNR						
5	7.5	4	0.5	6.67	0.02	0.6
10	16	6.2	5	8	0.05	2.93
15	20	5	9.8	12.3	12.4	3.05
20	18	5.5	15.2	13.9	9.5	4.58
25	17.6	5.4	13.1	13.3	3.5	5.1
Improve in spectral distortion						
5	49.5	−13.03	−4.17	−1.21	−5.35	−3.5
10	184	−23	−7	−2.2	−10.5	−9
15	4.88e3	−25	−3.95	−2.52	−1.0	−70
20	5.34e4	−36.4	−1.92	−1.4	−9.6	−37.5
25	5.65e5	−40	16.15	5.69	−164.5	−60.48
Improve in RMSE						
5	0.02	0.06	2.1e−3	0.023	1.6e−4	3.6e−3
10	0.044	0.082	−0.05	0.037	0.002	7e−3
15	0.102	0.10	0.07	0.085	0.08	0.016
20	0.17	0.098	0.145	0.164	0.137	0.06
25	0.32	0.114	0.28	0.243	0.031	0.12

Table 3
Improvement in FPR and TPR for proposed method in comparison with all other methods for different data RMS thresholds.

Trh, Data RMS	Proposed	wICA	wCCA	ICA	EMD-ICA	EMD-CCA
Improve in Avg. FPR (%)						
3	73.89	−1.68e3	−833.3	−241.17	−185.71	−57.14
4	95.24	−1.4e3	−699.6	−783.33	−587.5	−553.85
5	93.41	−1.28e3	−522.2	−1.02e3	−400	−1.16e3
6	90.91	−1.1e3	−474.7	−880.0	−337.5	−1.19e3
Improve in Avg. TPR (%)						
3	30.63	−92.21	−98.54	−84.93	−16.16	−5.93
4	14.93	−76	−98.0	−27.45	−34.37	−10.71
5	1.5	−91.43	−97.14	−56.41	−31.82	−31.82
6	10.46	−97.35	−96.3	−85.71	−71.43	−44.83

the algorithm induced spike-liked artifacts are present after signal reconstruction (Fig. 19). The best results among all the methods have been highlighted in blue for each SNR_{Art} level in Table 2.

Another problem with ICA and CCA related algorithms is the identification of artifacts from the independent components (ICs or CCs) which is first of all most of the time not automatic and secondly hard to identify as long as sufficient no. of recording channels is unavailable. However, wCCA seems to perform better than wICA since the sources are assumed to be maximally uncorrelated in CCA rather independent as in ICA which is a strong assumption. One important thing to note is that the performance of the algorithms do not follow any specific trend with respect to artifact SNR change, rather often it is found to be quite random. One possible reason of such random results is that because of the random locations of different artifact types, often they overlap in temporal domain, thus limits the outcome of the artifact removal method. Table 3 presents the false positive rate and true positive rate for spike detection before and after artifact removal of different methods compared with the proposed one. It is also clear that the proposed method has higher TPR and lower FPR than the other available methods. The values are given in terms of improve in FPR and TPR. The improvement in FPR, ΔFPR(%) and in TPR, ΔTPR(%) suggests that the no. of false positive decreases and the no. of true positive increases after artifacts are removed. The high negative values of ΔFPR(%) in Table 3 in other methods at almost all threshold values indicate that those methods highly induce spike-liked artifacts during the reconstruction process. However the proposed method significantly reduces the false positive rate except for threshold of 3 data RMS, even it is still much better than others. Regarding the improvement on TPR, the proposed method also outperforms all other methods significantly at all threshold levels. The best results have been highlighted in blue for each threshold level.

6. Conclusion

In this paper, we proposed an algorithm for artifact detection and removal which is based on the stationary wavelet transform with selected frequency bands of neural signals. The selection of frequency bands is based on the spectrum characteristics of in vivo neural data. Robustness of the proposed algorithm is further improved by a modified universal-threshold value. Both real and synthesized data have been used for testing the proposed algorithm in comparison with other available algorithms. Quantitative results showed that the proposed algorithm outperforms the others in removing artifacts reliably without distorting neural signals. Therefore, this work is expected to be useful for future research on proper preprocessing of *in vivo* neural signals. However, it also requires for further observations on experimental data to identify other artifacts (if any) and more importantly to model their sources, which is a non-trivial task. Our future work includes further optimization of the proposed algorithm and implementation for real-time applications.

Acknowledgments

The experiment data are provided by Victor Pikov at Huntington Medical Research Institute and Edward Keefer at Plexon Inc./University of Texas Southwest Medical Institute and with their permission to use.

The authors would like to acknowledge the funding support by A*STAR PSF Grant R-263-000-699-305, NUS YIA Grant R-263-000-A29-133, A*STAR-CIMIT R-263-000-A47-112 and MOE R-263-000-619-133.

Appendix A. Calculation of threshold parameters

The threshold parameters k_A and k_D are chosen based on artifact removal results from few initial trial/training cycles. If we sweep both these two parameters and evaluate the corresponding artifact removal performance in terms of the correlation value between signals before and after artifact removal, then we can get a rough idea of choosing the optimal values for k_A and k_D. In order to do so, we assume that the correlations between artifactual and reconstructed signals are higher in non-artifactual regions and lower in artifact-contaminated regions.

If $R_{XY_{Art}}$ and $R_{XY_{Non-Art}}$ are the correlation values between artifactual and reconstructed signals for artifact-contaminated regions (i.e. ID_i is artifact index) and non-artifact-contaminated regions (i.e. ID_i is not artifact index) respectively, then the optimization problem will be as follows:

- Find k_A for maximum $R_{XY_{Non-Art}}$ and minimum $R_{XY_{Art}}$.
- Find k_D for maximum $R_{XY_{Non-Art}}$ and minimum $R_{XY_{Art}}$.

Now if $k_{A_{\max}}$ be the value when $R_{XY_{Non-Art}}$ is maximum and $k_{A_{\min}}$ be the value when $R_{XY_{Art}}$ is minimum, then the optimal value of k_A (i.e. $k_{A_{opt}}$) is chosen as the average of these two values as given by following equation:

$$k_{A_{opt}} = \frac{k_{A_{\max}} + k_{A_{\min}}}{2} \tag{21}$$

Similarly the optimal value of k_D, (i.e. $k_{D_{opt}}$) is calculated as follows:

$$k_{D_{opt}} = \frac{k_{D_{\max}} + k_{D_{\min}}}{2} \tag{22}$$

The value of m can be averaged over few initial trials of 1-sec data segment from the following equation:

$$m = \frac{1}{N}\sum_{j=1}^{N} \frac{\max(|A_{10}|_j)}{(sd(A_{10})_j}. \tag{23}$$

References

Belitski A, Gretton A, Magri C, Murayama Y, Montemurro MA, Logothetis NK, Panzeri S. Low-frequency local field potentials and spikes in primary visual cortex convey independent visual information. Journal of Neuroscience 2008];28(22):5696–709.

Bar-Hillel A, Spiro ASE. Spike sorting: Bayesian clustering of non-stationary data. Advances in Neural Information Processing Systems 2005];17:105–12.

Beylkin G. On the representation of operators in bases of compactly supported wavelets. SIAM Journal on Numerical Analysis 1992];29(6):1716–40.

Buzsáki G, Anastassiou CA, Koch C. The origin of extracellular fields and currents – EEG, ECoG, LFP and spikes. Nature Reviews Neuroscience 2012];13(6):407–20.

Castellanos NP, Makarov VA. Recovering EEG brain signals: artifact suppression with wavelet enhanced independent component analysis. Journal of Neuroscience Methods 2006];158(2):300–12.

Chandra ROL. Detection, classification, and superposition resolution of action potentials in multiunit single-channel recordings by an on-line real-time neural network. IEEE Transactions on Biomedical Engineering 1997];44(5):403.

Coifman RR, Donoho DL. Translation-invariant denoising. Berlin, Germany: Springer-Verlag; 1995]. p. 125–50.

Dayan P, Abbott LF. Theoretical neuroscience: computational and mathematical modeling of neural systems. Cambridge, MA, USA: MIT Press; 2005].

Delorme A, Sejnowski T, Makeig S. Enhanced detection of artifacts in EEG data using higher-order statistics and independent component analysis. NeuroImage 2007];34(4):1443–9.

Eichenbaum H. The hippocampus and declarative memory: cognitive mechanisms and neural codes. Behavioural Brain Research 2001];127(12):199–207.

Flexer A, Bauer H, Pripfl J, Dorffner G. Using ICA for removal of ocular artifacts in EEG recorded from blind subjects. Neural Networks 2005];18(7):998–1005.

Foffani G, Moxon K. Decoding the spatio-temporal localization of behavioral events in populations of neurons. In: Conference proceedings. First international IEEE EMBS conference on neural engineering; 2003]. p. 24–7.

Fonseca-Pinto R. A new tool for nonstationary and nonlinear signals: The Hilbert-Huang transform in biomedical applications. In: Laskovski AN, editor. Chapter in biomedical engineering, trends, researches and technologies. Croatia: In-Tech; 2010].

Gao H-Y. Wavelet shrinkage denoising using the non-negative garrote. Journal of Computational and Graphical Statistics 1998];7(4):469–88.

Guerrero-Mosquera C, Navia-Vazquez A. Automatic removal of ocular artefacts using adaptive filtering and independent component analysis for electroencephalogram data. IET Signal Processing 2012];6(2):99–106.

Kaneko H, Suzuki HT. Tracking spike-amplitude changes to improve the quality of multineuronal data analysis. IEEE Transactions on Biomedical Engineering 2007];54(2):262–72.

Hsu W-Y, Lin C-H, Hsu H-J, Chen P-H, Chen I-R. Wavelet-based envelope features with automatic {EOG} artifact removal: application to single-trial EEG data. Expert Systems with Applications 2012];39(3):2743–9.

Islam MK, Tuan NA, Zhou Y, Yang Z. Analysis and processing of in vivo neural signal for artifact detection and removal. In: BMEI 2012 – 5th international conference on biomedical engineering and informatics; 2012]. p. 437–42.

Keefer EW, Botterman BR, Romero MI, Rossi FA, Gross GW. Carbon nanotube-coated electrodes improve brain readouts. Nature Nanotechnology 2008];39:434–9.

Lewicki M. A review of methods for spike sorting: the detection and classification of neural action potentials. Network: Computation in Neural Systems 1998];9:53–78.

Lytton W. From computer to brain: foundations of computational neuroscience. New York: Springer; 2002].

Mallat S. A Wavelet tour of signal processing: the sparse way. 3rd ed. California, USA: Academic Press; 2008].

Mitra P, Bokil H. Observed brain dynamics. New York: Oxford University Press; 2008].

Moen H. Wavelet transforms and efficient implementation on the GPU. Department of Informatics, University of Oslo; 2007], Master Thesis.

Molavi B, Dumont G. Wavelet based motion artifact removal for functional near infrared spectroscopy. In: Engineering in medicine and biology society (EMBC), 2010 annual international conference of the IEEE; 2010]. p. 5–8.

Molla MKI, Islam MR, Tanaka T, Rutkowski TM. Artifact suppression from EEG signals using data adaptive time domain filtering. Neurocomputing 2012];97:297–308.

Molle M, Yeshenko O, Marshall L, Sara SJ, Born J. Hippocampal sharp wave-ripples linked to slow oscillations in rat slow-wave sleep. Journal of Neurophysiology 2006];96(1):62–70.

Raghavendra BS, Dutt DN. Wavelet enhanced CCA for minimization of ocular and muscle artifacts in EEG. World Academy of Science, Engineering and Technology 2011];57(6 Dec):1027–32.

Rong F, Contreras-Vidal JL. Magnetoencephalographic artifact identification and automatic removal based on independent component analysis and categorization approaches. Journal of Neuroscience Methods 2006];157(2):337–54.

Harrison RR. A low-power integrated circuit for adaptive detection of action potentials in noisy signals. In: Annual international conference of the IEEE engineering in medicine and biology proceedings; 2003]. p. 3325–8.

Safieddine D, Kachenoura A, Albera L, Birot G, Karfoul A, Pasnicu A, Biraben A, Wendling F, Senhadji L, Merlet I. Removal of muscle artifact from EEG data: comparison between stochastic (ICA and CCA) and deterministic (EMD and wavelet-based) approaches. EURASIP Journal of Advances in Signal Processing 2012];2012:127.

Savelainen A. An introduction to EEG artifacts. In: Independent research project in applied mathematics. Finland: School of Science – Aalto University; 2010].

Savelainen A. Movement artifact detection from electroencephalogram utilizing accelerometer. Helsinki, Finland: School of Science and Technology, Aalto University; 2011], M.S. Thesis.

Scott B. Developments in EEG analysis, protocol selection, and feedback delivery. Journal of Neurotherapy 2011];15(3):262–7.

Snider RBA. Classification of non-stationary neural signals. Journal of Neuroscience Methods 1998];84(1–2):155–6.

Sweeney KT, McLoone SF, Ward TE. The use of ensemble empirical mode decomposition with canonical correlation analysis as a novel artifact removal technique. IEEE Transactions on Biomedical Engineering 2013];60(1):97–105.

Sweeney KT, Ward TE, McLoone SF. Artifact removal in physiological signals – practices and possibilities. IEEE Transactions on Information Technology in Biomedicine 2012];16(3):488–500.

Tomko G, Crapper D. Neuronal variability: non-stationary responses to identical visual stimuli. Brain Research 1974];79(3):405–18.

Wang YL, Liu JH, Liu YC. Automatic removal of ocular artifacts from electroencephalogram using Hilbert-Huang transform. In: ICBBE 2008 – The 2nd international conference on bioinformatics and biomedical engineering; 2008]. p. 2138–41.

Wang Y, Sanchez JC, Principe JC, Mitzelfelt JD, Gunduz A. Analysis of the correlation between local field potentials and neuronal firing rate in the motor cortex. In: Annual international conference of the IEEE engineering in medicine and biology proceedings; 2006]. p. 6185–8.
Winkler I, Haufe S, Tangermann M. Automatic classification of artifactual ICA-components for artifact removal in EEG signals. Behavioral and Brain Functions 2011];7(1):1–15.
Yang Z, Zhao Q, Keefer E, Liu W. Noise characterization, modeling, and reduction for in vivo neural recording. In: Bengio Y, Schuurmans D, Lafferty JD, Williams CKI, Culotta A, editors. NIPS. New York, USA: Curran Associates Inc.; 2009]. p. 2160–8.
Yang XSS. A totally automated system for the detection and classification of neural spikes. IEEE Transactions on Biomedical Engineering 1988];35(10): 806–16.
Yong X, Fatourechi M, Ward R, Birch G. Automatic artifact removal in a self-paced hybrid brain–computer interface system. Journal of Neuroengineering and Rehabilitation 2012];9(1):1–20.
Zhang L, Wu D, Zhi L. Method of removing noise from EEG signals based on hht method. In: ICISE 2009 – 1st International Conference on Information Science and Engineering; 2009]. p. 596–9.
Zhao C, Qiu T. An automatic ocular artifacts removal method based on wavelet-enhanced canonical correlation analysis. In: Engineering in Medicine and Biology Society, EMBC 2011 – Annual International Conference of the IEEE; 2011]. p. 4191–4.
Zima M, Tichavsk P, Paul K, Krajca V. Robust removal of short-duration artifacts in long neonatal EEG recordings using wavelet-enhanced ICA and adaptive combining of tentative reconstructions. Physiological Measurement 2012];33(8):N39.